Article

Determining Vortex-Beam Superpositions by Shear Interferometry

Behzad Khajavi[1], Junior R. Gonzales Ureta [1,2] and Enrique J. Galvez [1]

[1] Department of Physics and Astronomy, Colgate University, Hamilton, New York, U.S.A.
[2] Departamento de Ciencias, Sección Física, Pontificia Universidad Católica del Peru, Lima, Peru
* Correspondence: egalvez@colgate.edu; Tel.: +1-315-228-7205

Abstract: Optical modes bearing optical vortices are important light systems in which to encode information. Optical vortices are robust features of optical beams that do not dissipate upon propagation. Thus decoding the modal content of a beam is a vital component of the process. In this work we present a method to decode modal superpositions of light beams that contain optical vortices. We do so using shear interferometry, which presents a simple and effective means of determining the vortex content of a beam, and extract the parameters of the component vortex modes that constitute them. We find that optical modes in a beam are easily determined. Its modal content can be extracted when they are of comparable magnitude. The use of modes of well defined topological charge but not well defined radial-mode content, such as those produced by phase-only encoding, are much easier to diagnose than pure Laguerre-Gauss modes.

Keywords: Optical Vortices; Topological charge; Shear interference; Mode superposition

0. Introduction

Optical vortices are singular points contained in the transverse mode of beams of light. Around them the phase of the light waves advances by an integer multiple of 2π. They have attracted much attention in the last 25 years especially due to the intrinsic orbital angular that they carry in the field surrounding the optical vortex [1]. Many applications of optical vortices have been found [2], and among them, the encoding of information for communication purposes, both classical [3,4] and quantal [5,6]. Spatial modes have become attractive for bearing information because optical vortices are particularly robust in retaining their character as the light propagates through media and turbulence [7,8]. The promise of this approach is the enhanced space of information bits, well beyond binary, and in principle unbound. Encoding can be done by use of vortices as an incoherent alphabet for communicating information [9] or as coherent superpositions of modes in a deliberate way [10] as a high-dimensional basis of states [11].

These developments have led to a number of methods to encode and decode optical-vortex structures in beams. In this work we devote to the detection of the vortex content of beams. Numerous methods have been developed for the detection of optical modes of a beam bearing an optical vortex. They include non-collinear interferometry of the beam with itself [12], or in nested interferometers bearing parity-changing optical elements [13], or more simply with single optical elements, such as a double slit [14], a single slit [15], a triangular aperture [16], cylindrical lenses [17], conformational optics [18] or use of a shear interferometer [19]. Beyond a beam carrying a singly or multiply charged vortex, it is quite necessary to be able to detect superpositions or to be able to sort the modal content of beams. Promising approaches include the use of projecting modes into the fundamental gaussian mode [5], or by unwrapping modes via conformational optics to spatially separate them [18,20]. A more conventional approach is one that uses shear interferometry to recognize the vortex [21]. We use also use shear interference by single element, an extension of a method developed by two of us [19]. In this article we present the application of shear interferometry to determine modal superpositions of vortex beams. We start with the theoretical underpinnings,

1. Theory

1.1. Modal Structure

Collinear superpositions of paraxial beams bearing optical vortices produce a composite mode that can be diagnosed to determine through the vortices the composition of the modes in it. This is due to a basic feature of vortex beams: The modal pattern consists of a brightest inner ring with a radius that depends on the topological charge ℓ:

$$r_\ell \propto \ell^a, \tag{1}$$

where a is a positive number. For pure Laguerre-Gauss beams $r_\ell = (\ell/2)^{1/2} w$, where w is the beam half width.

Let us assume that the superposition of the vortex modes is given by

$$u = \cos\beta\, u_{\ell_1} + \sin\beta\, u_{\ell_2} e^{i\gamma}, \tag{2}$$

where ℓ_1 and ℓ_2 are the topological charges of the two modes, β specifies the ratio of the amplitudes of the two modes and γ is their relative phase. The functional expression for the modes is given by u_ℓ. We can distinguish two cases.

- When $|\ell_1| < |\ell_2|$, the modal pattern is quite predictable and showing the following features:
  - The center of the pattern has an optical vortex of charge ℓ_1. This is what is theoretically predicted. In practice, a multiply charged point is very susceptible to perturbations, and so the center of the pattern may consist of $|\ell_1|$ singly charged vortices of sign $\ell_1/|\ell_1|$ in close proximity.
  - The center is surrounded by $|\ell_1 - \ell_2|$ vortices arranged symmetrically about the center [22], and at a distance r_v that satisfies
  $$\tan\beta = \frac{|u_{\ell_1}|}{|u_{\ell_2}|}. \tag{3}$$
  For the case of pure Laguerre-Gauss modes, we know the analytical expressions of u_ℓ, and so we can deduce r_v:
  $$r_{v,LG} = \frac{w}{\sqrt{2}} \left(\frac{|\ell_2|!}{|\ell_1|!\tan^2\beta} \right)^{\frac{1}{2(|\ell_2|-|\ell_1|)}}. \tag{4}$$
  The position of the vortices depends on the relative phase between the two modes [22]
  $$\phi_v = \frac{\gamma + n\pi}{\ell_2 - \ell_1}, \tag{5}$$

  For example, when $\ell_1 = +1$ and $\ell_2 = -2$, the composite mode for $\beta = 45°$ consists of a central vortex of charge $+1$ surrounded by 3 vortices of charge -1 located at a radius r_v.
- When $\ell_1 = -\ell_2$ the pattern contains a central vortex of charge $\ell_1/|\ell_1|$ at $\beta \neq 45°$. At $\beta = 45°$ there is no central vortex. The composite mode has $2|\ell_1|$ radial lines of 180° shear phase, symmetrically separated. The relative weights of the modes produce on subtle variations in intensity, which yields greater uncertainty in the determination. The method presented here is much more effective for the previous case.

1.2. Shear Interference Pattern

For a pure mode ℓ, the shear interferometry of beams bearing optical vortices produces a pattern with the following characteristics [19]:

- The pattern consists of conjoined vortices. If the shear interferometer is air spaced, the centers of the vortices are displaced by
$$s = 2t\sin\alpha, \tag{6}$$

Peer-reviewed version available at *Photonics* **2018**, *5*, 16; doi:10.3390/photonics5030016

where α is the incident angle, and t is the average thickness traversed by the beam. This relation is modified if the fringes are not parallel to the displacement of the two modes.

- The overall phase of the pattern is determined by the optical path-length difference and the reflection phases, which for our case is given by

$$\psi = \frac{4\pi t \cos\alpha}{\lambda} + \pi. \tag{7}$$

- The fringe density of the pattern is given by

$$\rho \simeq \frac{\theta}{\lambda}, \tag{8}$$

where θ is the angle that the back reflection makes with the horizontal, where $\theta > 0$ when the back reflection is tilted downward, and assuming that the front reflection is in the horizontal plane. It is given by

$$\theta = 2\delta\cos\alpha, \tag{9}$$

where δ is the wedge angle between the two active surfaces.

When the interferometer is a solid piece, which we have used in the past [19,23], these relations are modified slightly [24]. We found air-spaced interferometers very convenient for freely changing the above parameters. In a typical situation aiming for a total of 15 fringes over the full size of the beam of 4 mm, with $\alpha = 45°$ requires a tilt $\delta \sim 5.8$ arcmin. The pattern representing an optical vortex consists forks joined by their handles or their tines when the topological charge is positive or negative, respectively, as discussed below. These patterns invert when $\theta < 0$.

2. Results

2.1. Mode Comparison

The effectiveness of the method depends on the radial dependence of the vortex mode. The "fuller" the mode, the better. This is because the pattern is the interference of two displaced identical modes. Such modes are the ones generated, for example, with a spiral phase plate or a forked diffraction grating, and known also as Hypergeometric-Gaussian modes [25]. Laguerre-Gauss eigenmodes are categorized by two indices: the azimuthal index or topological charge ℓ , and the radial index p specifying the number of nodes in the radial coordinate. Pure $p = 0$ eigenmodes are the hardest to diagnose. This is because most of the light intensity is limited to a well defined ring, and so the signal to noise of the interference patterns is low in the dark regions. Hypergeometric-Gaussian modes generated by phase-only encoding are in a superposition of Laguerre-Gauss modes of same ℓ but different p [26]. Such modes modes have intensity patterns featuring a main ring surrounded by broad radial modulations. They are much better because most regions of overlap of the modes are well lit and thus produce good fringe visibilities. When investigations are limited to a laboratory area, it is often convenient to image the mode encoding element via a 4-f sequence of lenses. That way the beam reconstructed onto the camera is nearly a Gaussian (the input to the encoding device), with the phase encoding. Imperfections in the encoding, imaging apparatus and diffraction itself make the modes with distinct topological charge be distinct as well, enabling optical processing with such modes. We cal this type of imaging "near field."

Figure 1 shows three types of modes that we prepared with a spatial light modulator, and their corresponding shear interference pattern below. They were taken with our air-spaced interferometer that allowed us to adjust the plate separation. The modes were generated by diffraction off the phase grating of a spatial light modulator with and without amplitude modulation. The amplitude modulation produces a pure Laguerre-Gauss mode, while the lack of amplitude modulation produces a Hypergeometric-Gauss mode as described above. Pure $p \neq 0$ eigenmodes are much harder to determine because they contain more than one ring, and with consecutive rings being π out of phase. This feature complicates the pattern produced by the shear interferometer. The darkened regions

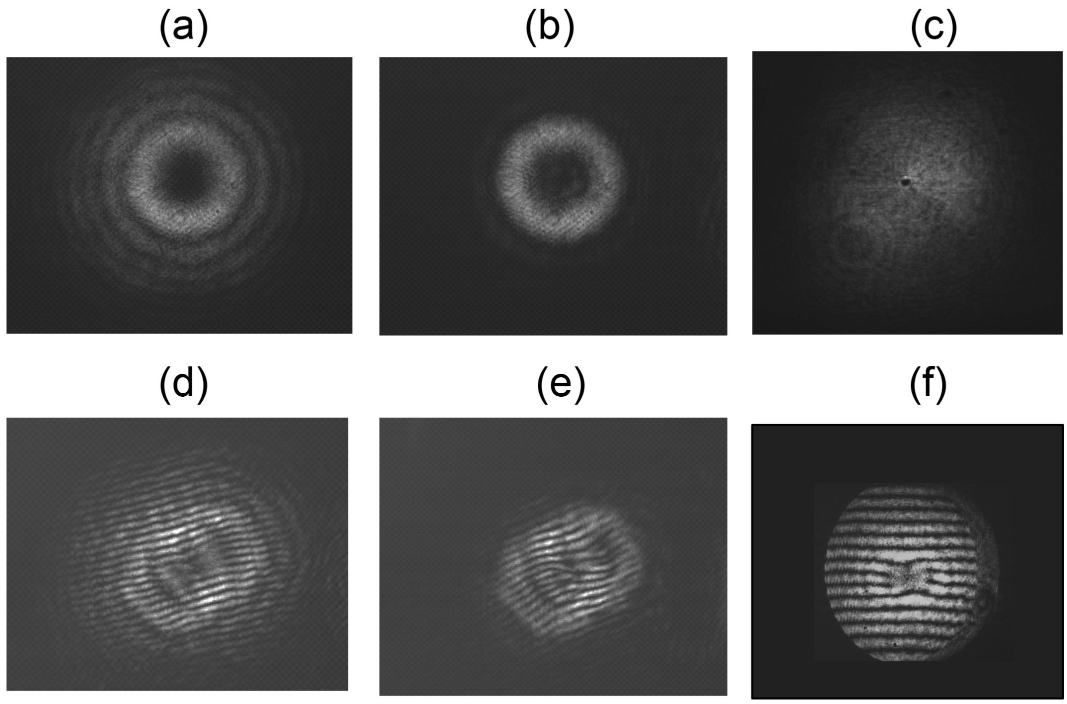

Figure 1. Beam modes (a-c) and corresponding shear interferograms (d-f) of vortex beams generated using phase modulation only (a,c), phase and amplitude modulation (b); and far-field (a,b) and near-field imaging (c). All modes have $\ell = +2$.

in the modes of Fig. 1(a-c) are candidates for locations bearing optical vortices , but only the shear interference pattern can confirm this association of darkened regions with vortices. It can be seen that the fuller the beam, the clearer the pattern.

2.2. Varying the Topological Charge

The main virtue of the method presented in this article involves identifying vortex-mode superpositions. When this involves equal-amplitude superpositions ($\beta = 45°$ in Eq. 2), we can clearly determine the modes, regardless of the type of mode. Beyond inspecting the static images of the patterns, we can determine the relative phase of each image point by slightly varying the incident angle α of the light onto the shear interferometer, and fitting the phase of the pattern, as described below. We show such a sequence in Movie1.

Figure 2 shows the example of the superposition of $\ell_1 = +1$ with $\ell_2 = -2$ ($\beta = 45°$). We use a near-field pattern to best appreciate the procedure. We first identify the vortices. The modes are determined using the following procedure:

- We first examine the fork pattern in the center of the mode. From it we extract the magnitude $|\ell_1|$ and sign $\sigma_1 = \ell_1|/|\ell_1|$ of the mode with smaller topological charge. No vortices means $\ell_1 = 0$. In the case of Fig. 2(b) we see a $+1$ conjoined fork, revealing that one of the modes is $\ell_1 = +1$. In the table in Fig. 2(a) we give the correspondence between the sign of the topological charge of the vortex and its signature in the shear pattern.
- We count the number of peripheral vortices N. (In Fig. 2(b) we see that $N = 3$). Their sign is specified by the type of conjoined forks. If the sign is the same as the one at the center, then

$$\ell_2 = \sigma_1 (N + |\ell_1|) \,. \tag{10}$$

If the sign of peripheral vortices is different than the center vortex (as is the case of Fig. 2(b)), then

$$\ell_2 = -\sigma_1 \left(N - |\ell_1|\right). \tag{11}$$

In our example, because the sign of the peripheral vortices is different from the one of the central vortex, we conclude that $\ell_2 = -2$.

- The angular orientation of the vortices reveals the relative phase between the modes per Eq. 5. In our example, $\gamma \sim 0$ or π. The ambiguity is due to the uncertainty in the parity inversion that mirror-inverts the pattern. This uncertainty also arises when the patterns are mirror invariant (i.e., giving rise to N even).

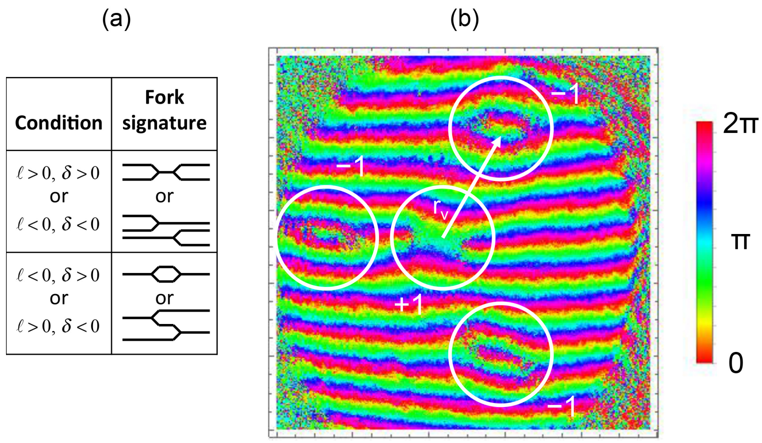

Figure 2. (a) Table showing the conditions that lead to distinct shear patterns of optical vortices. $\delta > 0$ corresponds to the second reflection deflected downward relative to the first reflection off the shear interferometer. (b) Phase pattern of the shear interference of the superposition of modes with topological charges $\ell_1 = +1$ and $\ell_2 = -2$. We label the arrangement of vortices produced by the superposition. The measured radial distance of the vortices r_v is taken as the distance between the center of the central pattern and the center of each of the peripheral vortices.

Figure 3 shows 4 cases with distinct values of (ℓ_1, ℓ_2): $(1, -2)$, $(1, -4)$, $(2, -4)$, and $(-1, -2)$. The

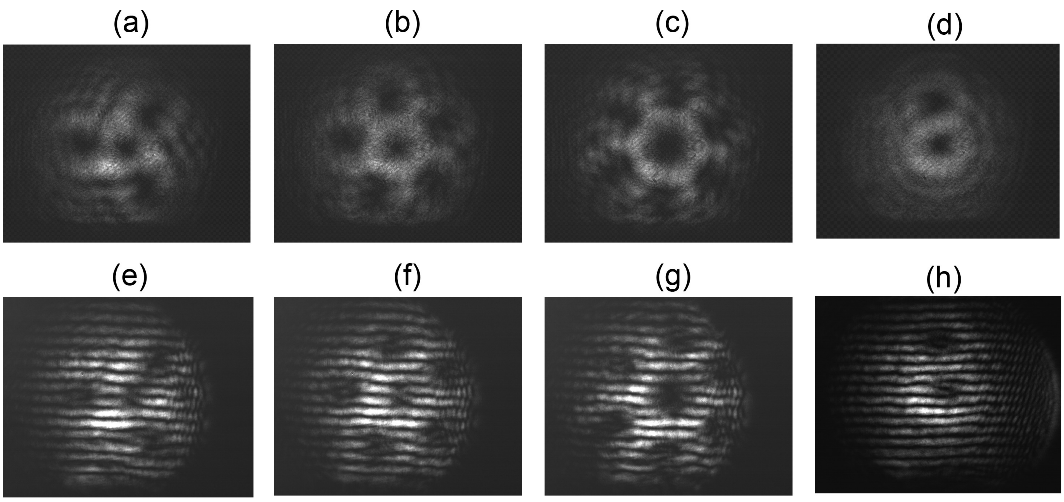

Figure 3. Images of equal-amplitude superpositions of modes with topological charges $(1, -2)$ in (a), $(1, -4)$ in (b), $(2, -4)$ in (c), and $(-1, -2)$ in (d). The images in the second row (e-h) are the shear interferograms of the superpositions above them.

Peer-reviewed version available at *Photonics* **2018**, *5*, 16; doi:10.3390/photonics5030016

figure shows views of the raw modes in panes (a-d) and the shear interferograms in (e-h). All cases were taken in the far field produced by the non-amplitude modulated encoding. The raw modes show dark regions where the vortices are located. The presence of a vortex is only confirmed by the appearance of the forked dislocations in the interferograms. The first case (a,e) is similar to the one in Fig. 2(b), featuring one central +1 vortex surrounded by three -1 vortices. The second case $(\ell_1, \ell_2) = (1, -4)$ in (b,f) has again a central $+1$ vortex surrounded by five -1 vortices. The third case with $(2, -4)$ underscores the method, showing a $+2$ central vortex, surrounded by 6 -1 vortices. The case $(-1, -2)$ involves $\gamma = \pi/2$. When $\gamma = 0, \pi$ the peripheral vortex is along the horizontal axis of the pattern.

When the fringes are lined up along the location of the displaced modes, positive vortices are revealed by two forks connected by their handle, whereas negative vortices are revealed by two forks conjoined by the tines. If the alignment is not as good, then the conjoined forks are laterally displaced, as illustrated in Fig. 2(a), so that for example, in the case of negative vortices, the forks share only one tine. They can also share no tines and just be laterally displaced. We can also make adjustments to a second tilt of the air-spaced interferometer to tilt the fringes along the direction that connects the displaced vortices. The case of Fig. 2(b) shows clearly that the forks representing each vortex are joined by both tines. Depending on the value of the local phase difference between the two interference beams, the forks are more clearly observed either via the bright or dark fringes.

2.3. Varying β

The comparisons of the previous cases involve equal-amplitude superpositions. The question that begs is: To what degree can this method detect superposition of modes with unequal amplitudes? We can determine the superposition as long as we can have light from one reflection of the shear interferometer overlap with all vortex locations of the second reflection, and vice versa. Such a situation is the requirement for producing a measurable fork pattern. In the case of the pure eigenmodes, the settings of the shear interferometer (separation and tilt) have to be adjusted for the particular situation, whereas in the fuller non-eigenmodes, no specific settings are required.

The peripheral vortices that surround the central vortex, located at a radius r_v, are seen as long as $r_v < R$, where R is the visible radius of the beam. This sets a lower bound for the value of $\beta = \beta_{\text{min}}$ in Eq. 2, which depends on the type of vortex mode: lower for fuller modes. In the cases that we investigated $\beta_{\text{min}} \sim 35°$. Figure 4 shows an example of modes created with unequal amplitudes. We show in pane (a) the case with $(+1, -2)$ with $\beta = 35°$. The peripheral vortices are close to the edge of the beam. Depending on the type of mode, this minimum value can range between 30° and 40°.

In similar manner, as $\beta \to 90°$ the singly charged vortices reach the center to form a region of charge ℓ_2. For $\beta > \beta_{\text{max}}$, it is not possible to distinguish clearly the central vortex from the peripheral vortices, and so we cannot identify the component modes. From our own experience, $\beta_{\text{max}} \sim 70°$. Figure 4(c) shows the case for $\beta = 60°$. We have taken sequences of a number of cases with varying ℓ_1, ℓ_2 and β. In Movie2 we show a case for a sequence of β values.

We further did an analysis of the variation of r_v with β by measuring the values of r_v in the images. In Fig. 5 we show the case of $(+1, -2)$. We divide the value of r_v by the radius of the beam R. The uncertainties are standard deviations of the measurements. We compare those measurements with the predicted value of $r_v = r_{v-LG}$ scaled by a factor of $\sqrt{2}$. We found similar agreement with two other cases that we studied, but using other scalings.

3. Discussion

The analysis shown above shows that shear interferometry can be used to identify the topological charges of modes in superpositions. We can do this determination for most pure or semi-pure modes bearing optical vortices. We have showed this with modes imaged in the far field as well as in the near field [23]. The method can be used to determine the relative weights of the two modes when their

Preprints (www.preprints.org) | NOT PEER-REVIEWED | Posted: 17 May 2018 doi:10.20944/preprints201805.0252.v1

Peer-reviewed version available at Photonics 2018, 5, 16; doi:10.3390/photonics5030016

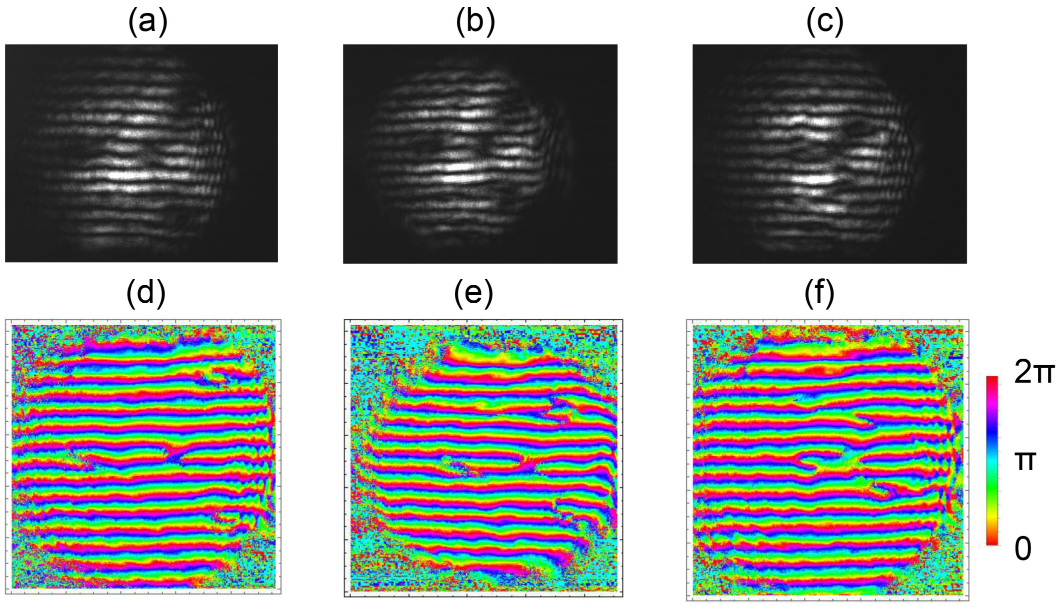

Figure 4. Top row: Shear interferograms of the superposition of modes with topological charges $\ell_1 = +1$ and $\ell_2 = -2$ for several values of β: 35° in (a),45° in (b) and 60° in (c). Bottom row: reconstructions of the phase of the light field corresponding to the shear patterns above them. False color encodes phase.

amplitudes are not too dissimilar (in the language of Eq. 2, for $30^\circ \leq \beta \leq 70^\circ$. The results of this article apply for modes in the far field, which may be used in communications. If the use of vortex beams is limited to the laboratory environment, one can use engineered near-field patterns, which allow greater flexibility in the encoding of vortices[10] and greater ease in their detection by shear interferometry [23].

Our analysis works for modes that do not involve phase changes in the radial directions. That is, for example, $p = 0$ Laguerre-Gauss modes. Modes with predominantly $p > 0$ have π-phase inversions at radial nodes. Our simulations show that superpositions of these types of modes lead to a duplication of the peripheral vortices for each radial node, yielding very complicated patterns with numerous vortices that may be very difficult to unravel.

The identification of modal superpositions done here was done with an air-spaced shear interferometer that we built. This gives much flexibility in adjusting the characteristics of the pattern

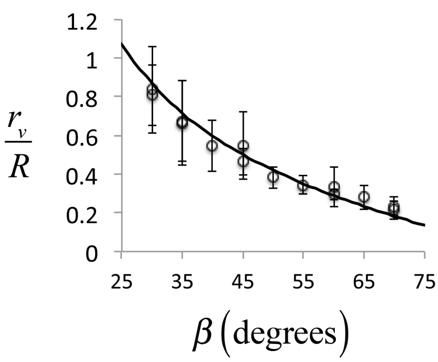

Figure 5. Graph of the radial position of the peripheral vortices relative to the beam radius as a function of the parameter β that determines the ratio of the amplitudes of the modes in Eq. 2. The data shown corresponds to the case $(+1, -2)$. The solid line corresponds to the $r_{v-LG}/(\sqrt{2}w)$ in Eq. 4.

 doi:10.20944/preprints201805.0252.v1

Peer-reviewed version available at *Photonics* **2018**, *5*, 16; doi:10.3390/photonics5030016

that best suit the modal determinations. Such freedom allows the adjustment of the interferometer angles. These determinations can also be done with a commercially available single-plate shear interferometer, as reported recently [19,23].

4. Apparatus and Methods

4.1. Shear Interferometer

In this work we used an air-spaced shear interferometer shown in the insert to Fig. 6. It consisted of two thick (~ 5 mm) uncoated wedged glass blanks mounted in such a way that the one responsible for the back reflection was mounded in a mirror-type mount so that its tilt δ could be adjusted. The blank responsible for the first reflection, made of vycor glass ($n = 1.438$), was mounted on a translating mount to enable adjustment of the separation between the two active surfaces t. The entire interferometer was mounted on a rotation stage that allowed for slight variations in the incident angle α. We used the latter to change the phase ψ between the two reflections. The data was taken for an angle of incidence of about $\alpha = 45°$, which corresponds to an internal angle of incidence on the shear gap of 29°.

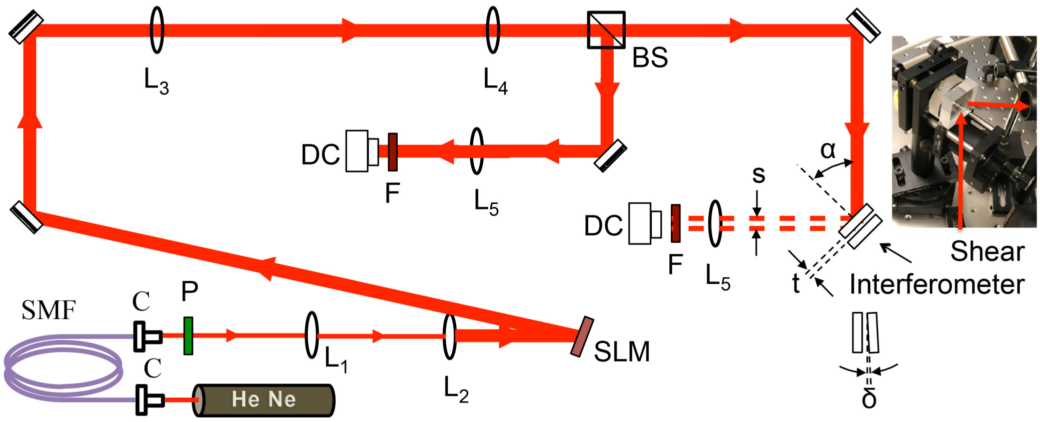

Figure 6. Apparatus used to make the measurements. Components include spatial light modulator (SLM) lenses (L_i), fiber collimators (C), single-mode fiber (SMF), beam splitter (BS), polarizer (P), neutral density filters (F), and digital camera (DC). Insert shows a photo of the shear interferometer. The diagram also shows the relevant parameters of the interferometer: the angle of incidence α, the shear displacement s, the shear-plate separation t, and second plate tilt δ.

The entire layout of our optical setup is shown in Fig. 6. The output of a helium-neon laser is spatially filtered by passage through a single-mode fiber (SMF) coupled by collimators (C). The polarization of the beam is adjusted for optimal diffraction with a spatial light modulator (SLM). The light incident on it is expanded via lenses F_1 and F_2. The first-order diffraction off the SLM is expanded further with lenses F_3 and F_4 and divided by a beam splitter to observe the mode with digital camera. The second beam expansion was needed for greater overlap of the two shear reflections. The light transmitted by the beam splitter was steered onto the shear interferometer. We also used a single-element shear interferometer to insure that the input beam had a maximum radius of curvature. The beam bearing the shear interference pattern was slightly focused by a lens to fit the mode within the digital camera sensing element.

4.2. Shear-Pattern Analysis

The shear interferometer has the flexibility to allow the change in the phase of the interference pattern by sightly varying the incident angle α: 3 arcmin change per fringe shift using Eq. 7. As mentioned above, we collected a movie of the pattern for at least one fringe shift. We used this data to fit the period of the pattern in a sequence of images. The outcome of that fit was used as a fixed parameter to fit the phase of each imaged point. The outcome of this analysis yielded the phase patterns of the type shown in Figs. 2 and 4. The phase of the pattern allows a straightforward determination of the vortices, and from them we can find the topological charge of the component beams. We used this procedure as an alternative to the determination of vortices directly from the interferograms. This procedure can be automated further using an algorithm to make an automatic determination of the location of the vortices and their topological charge.

5. Conclusions

To conclude, we presented a robust method to determine the topological charges of modal superpositions based on shear interferometry. The method relies on the interference of an incoming beam with itself, so it does not rely on the need for a reference beam. The key aspect of the method is that it is simple and robust. Optical vortices arrange in a predictably way that can be used to make the modal determinations. This includes a range of the relative weights of the 2 vortex modes in the superposition and their relative phase. The method presented here can be used to identify vortex modes when they are inserted in optical beams for the purpose of encoding information. This method may also be used as a diagnosis tool when using optical vortices in biomedical diagnosis or nanotechnology.

Author Contributions: Individual contributions: Conceptualization and Methodology, B.K. and E.G.; Data Acquisition B.K., J.G.; Analysis, B.K., J.G., E.G.; Writing, E.G.

Funding: This research was funded by the National Science Foundation grant number PHY1506321.

Conflicts of Interest: The authors declare no conflict of interest. The founding sponsors had no role in the design of the study; in the collection, analyses, or interpretation of data; in the writing of the manuscript, and in the decision to publish the results.

References

1. Allen, L.; Beijersbergen, M.; Spreeuw, R.; Woerdman, J. Orbital angular momentum of light and the transformation of Laguerre-Gaussian laser modes. *Phys. Rev. A* **1992**, *45*, 8185–8189.
2. et. al., H.R.D. Roadmap on structured light. *J. Opt.* **2017**, *013001*.
3. Gibson, G.; Courtial, J.; Padgett, M.; Vatnetsov, M.; Pas'ko, V.; Barnett, S.; Franke-Arnold, S. Free-space information transfer using light beams carrying orbital angular momentum. *Opt. Express* **2004**, *12*, 5448–5456.
4. Wang, J.; Yang, J.Y.; Fazal, I.M.; Ahmed, N.; Yan, Y.; Huang, H.; Ren, Y.; Yue, Y.; Dolinar, S.; Tur, M.; Willner, A.E. Terabit free-space data transmission employing orbital angular momentum multiplexing. *Nat. Photonics* **2012**, *340*, 488–496.
5. Mair, A.; Vaziri, A.; Weihs, G.; Zeilinger, A. Entanglement of the orbital angular momentum states of photons. *Nature* **2001**, *412*, 313–316.
6. Molina-Terriza, G.; Torres, J.; Torner, L. Twisted photons. *Nat. Phys.* **2008**, *3*, 305–310.
7. Malik, M.; O'Sullivan, M.; Rodenburg, B.; Mirhosseini, M.; Leach, J.; Lavery, M.P.J.; Padgett, M.; Boyd, R. Influence of atmospheric turbulence on optical communications using orbital angular momentum for encoding. *Opt. Express* **2012**, *20*, 13195–13200.
8. D'Ambrosio, V.; Nagali, E.; Walborn, S.; Aolita, A.; Slussarenko, S.; Marrucci, L.; Sciarrino, F. Complete experimental toolbox for alignment-free quantum communication. *Nat. Commun.* **2012**, *3*, 961.
9. Krenn, M.; Fickler, R.; Fink, M.; Handsteiner, J.; Malik, M.; Scheidl, T.; Ursin, R.; Zeilinger, A. Communication with spatially modulated light through turbulent air across Vienna. *New J. Phys.* **2014**, *16*, 113028.
10. Molina-Terriza, G.; Torres, J.; Torner, L. Management of the angular momentum of light: Preparation of photons in multidimensional vector states of angular momentum. *Phys. Rev. Lett.* **2002**, *88*, 013601.
11. Barreiro, J.; Langford, N.; Peters, N.; Kwiat, P. Generation of hyperentangled photon pairs. *Phys. Rev. Lett.* **2005**, *95*, 260501.

12. Heckenberg, N.; McDuff, R.; Smith, C.; Rubinsztein-Dunlop, H.; Wegener, M. Laser beams with phase singularities. *Opt. Quanum Electron.* **1992**, *24*, 355–361.
13. Leach, J.; Padgett, M.J.; Barnett, S.M.; Franke-Arnold, S.; Courtial, J. Measuring the orbital angular momentum of a single photon. *Phys. Rev. Lett.* **2002**, *88*, 257901.
14. Sztul, H.I.; Alfano, R.R. Double-slit interference with Laguerre-Gaussian beams. *Opt. Lett.* **2006**, *31*, 999–1001. doi:10.1364/OL.31.000999.
15. Ferreira, Q.; Jesus-Silva, A.; Fonseca, E.; Hickmann, J. Fraunhofer diffraction of light with orbital angular momentum by a slit. *Opt. Lett.* **2011**, *36*, 3106–3108.
16. Hickmann, J.; Fonseca, E.; Soares, W.; Chavez-Cerda, S. Unveiling a truncated optical lattice associated with a triangular aperture using light's orbital angular momentum. *Phys. Rev. Lett.* **2010**, *105*, 053904.
17. Beijersbergen, M.W.; Allen, L.; van der Veen, H.E.L.O.; Woerdman, J.P. Astigmatic laser mode converters and transfer of orbital angular momentum. *Opt. Commun.* **1993**, *96*, 123–132.
18. Berkhout, G.C.; Lavery, M.P.; Courtial, J.; Beijersbergen, M.W.; Padgett, M.J. Efficient sorting of orbital angular momentum states of light. *Phys. Rev. Lett.* **2010**, *105*, 153601.
19. Khajavi, B.; Galvez, E. Determining topological charge of an optical beam using a wedged optical flat. *Opt. Lett.*, *42*, 1516–1519.
20. O'Sullivan, M.; Mirhosseini, M.; Malik, M.; Boyd, R. Near-perfect sorting of orbital angular momentum and angular position states of light. *Opt. Express* **2012**, *20*, 24444.
21. Ghai, D.P.; Senthilkumaran, P.; Sirohi, R. Shearograms of an optical phase singularity. *Opt. Commun.* **2008**, *281*, 1315–1322.
22. Baumann, S.; Kalb, D.; MacMillan, L.; Galvez, E. Propagation dynamics of optical vortices due to Gouy phase. *Opt. Express* **2009**, *17*, 9818–9827.
23. Khajavi, B.; Galvez, E. Determination of the topological charge of complex light beams by shearing interference from a wedged optical at. *Proc. SPIE* **2018**, *10549*, 105490M.
24. Riley, M.E.; Gusinow, M.A. Laser beam divergence utilizing a lateral shearing interferometer. *Appl. Opt.* **1977**, *16*, 2753–2756.
25. Karimi, E.; Zito, G.; Piccirillo, B.; Marrucci, L.; Santamato, E. Hypergeometric-Gaussian modes. *Opt. Lett.* **2007**, *32*, 3053–3055.
26. Sephton, B.; Dudley, A.; Forbes, A. Revealing the radial modes in vortex beams. *Appl. Opt.* **2016**, *55*, 7830–7835.